

ESTIMATING THE PARAMETERS OF SGR A*'S ACCRETION FLOW VIA MILLIMETER VLBI

AVERY E. BRODERICK¹, VINCENT L. FISH², SHEPERD S. DOELEMAN² & ABRAHAM LOEB³*Draft version March 3, 2019*

ABSTRACT

Recent millimeter-VLBI observations of Sagittarius A* (Sgr A*) have, for the first time, directly probed distances comparable to the horizon scale of a black hole. This provides unprecedented access to the environment immediately around the horizon of an accreting black hole. We leverage both existing spectral and polarization measurements and our present understanding of accretion theory to produce a suite of generic radiatively inefficient accretion flow (RIAF) models of Sgr A*, which we then fit to these recent millimeter-VLBI observations. We find that *if* the accretion flow onto Sgr A* is well described by a RIAF model, the orientation and magnitude of the black hole's spin is constrained to a two-dimensional surface in the spin, inclination, position angle parameter space. For each of these we find the likeliest values and their 1- σ & 2- σ errors to be $a = 0^{+0.6+0.9}_{-0^{+0.6+0.9}}^{\circ}$, $\theta = 40^{+20+50}_{-0^{+20+50}}^{\circ}$, and $\xi = -23^{+35+110}_{-17^{+35+110}}^{\circ}$, when the resulting probability distribution is marginalized over the others. The most probable combination is $a = 0^{+0.2+0.4}_{-0^{+0.2+0.4}}^{\circ}$, $\theta = 90^{+7+10}_{-8^{+7+10}}^{\circ}$, though the uncertainties on these are very strongly correlated, and high probability configurations exist for a variety of inclination angles above 30° and spins below 0.99. Nevertheless, this demonstrates the ability millimeter-VLBI observations, even with only a few stations, to significantly constrain the properties of Sgr A*.

Subject headings: black hole physics — Galaxy: center — techniques: interferometric — submillimeter — accretion, accretion disks

1. INTRODUCTION

Understanding the structure and dynamics of black hole accretion flows has remained a central problem in astrophysics. Only in the past decade have sufficient numerical resources existed to perform self-consistent, three-dimensional magneto-hydrodynamic (MHD) simulations capable of resolving the magneto-rotational instability, believed to be responsible for angular-momentum transport in black-hole accretion flows. However, a true *ab initio* computation is still well beyond reach, resulting in the need for a variety of simplifying assumptions (e.g., the suitability of MHD, importance of electron-ion coupling, properties of accelerated electrons, etc.). As a result, the number of applicable models has rapidly proliferated, many of which are capable of describing the variety of phenomena observed. This is due in large part to the inability of current observations to resolve horizon scales. Unfortunately, the compact nature of black holes makes it very difficult to access the inner-edge of black hole accretion flows.

Sagittarius A* (Sgr A*), the bright radio point source coincident with the center of the Milky Way, is presently the best studied known black-hole candidate. Observations of orbiting OB-stars, the closest of which passes within 45 AU of Sgr A*, have produced a measured mass of $4.5 \pm 0.4 \times 10^6 M_{\odot}$ and an Earth-Sgr A* distance⁴ of 8.4 ± 0.4 kpc (Ghez et al. 2008). Already, there is

strong evidence for the existence of horizon in this source (Broderick & Narayan 2006; Broderick, Loeb & Narayan 2008). However, in many ways, Sgr A* is very different than the supermassive black holes in AGN. Unlike its active brethren, Sgr A* is vastly under-luminous, with a luminosity many orders of magnitude smaller than the Eddington luminosity. As a result, it is widely expected that Sgr A*'s accretion flow is quite different than that in AGN, though perhaps more indicative of the roughly 90% of supermassive black holes that are not presently in an active phase.

Even when strong-gravitational lensing is accounted for, the apparent angular size of Sgr A*'s horizon is only $55 \pm 2 \mu\text{as}$, a factor of two larger than the next largest black hole (M87) and orders of magnitude larger than any other known black hole (including all stellar-mass black holes). Nevertheless, despite its tiny angular size, recent millimeter VLBI experiments have successfully resolved this scale (Doeleman et al. 2008). Since only a handful of telescopes were involved with these observations, the resulting u - v coverage of the measured visibilities is very sparse. As a result only two simple models of Sgr A*'s image, a Gaussian and an annulus, were fit to the data by Doeleman et al. (2008).

However, we have a great deal of additional information about Sgr A*, including its spectral and polarization properties. We may also require physical consistency in any model (which would likely rule out an annulus, for example). Furthermore, we would like to evaluate the ability of, and optimize for this purpose, future millimeter and sub-millimeter VLBI experiments to constrain fundamental properties of the accretion flow in Sgr A*. This paper demonstrates the fitting and parameter estimation procedure for a simple radiatively inefficient accretion disk model (RIAF). In particular, we show that

¹ Canadian Institute for Theoretical Astrophysics, 60 St. George St., Toronto, ON M5S 3H8, Canada; aeb@cita.utoronto.ca

² Massachusetts Institute of Technology, Haystack Observatory, Route 40, Westford, MA 01886.

³ Institute for Theory and Computation, Harvard University, Center for Astrophysics, 60 Garden St., Cambridge, MA 02138.

⁴ The mass and distance measurements are strongly correlated, with mass scaling roughly as $M \propto D^{1.8}$.

even from very sparse baseline coverage it is possible to robustly extract interesting parameters of a generic RIAF. A study that considers how future high frequency VLBI observations can extend this work will be presented elsewhere (Fish et al. 2008).

In section 2 we summarize the VLBI observations that form the basis for our analysis. In 3 we present the simple accretion flow model that we employ. Sections 4 and 5 discuss the data fitting procedure, including the Bayesian method by which we do the parameter estimation, and the generic constraints placed by the current VLBI results. Section 6 details how we define our uncertainties and presents our parameter estimates. Finally, we conclude in section 7.

2. SUMMARY OF VLBI OBSERVATIONS

In April 2007, Sgr A* and several quasar calibrators were observed at a wavelength of 1.3mm with a three station VLBI array (Doeleman et al. 2008). The array included the James Clerk Maxwell Telescope (JCMT) on Mauna Kea, the Arizona Radio Observatory Submillimeter Telescope (ARO-SMT) on Mt. Graham in Arizona, and one 10m dish of the Coordinated Array for Research in Millimeter-wave Astronomy (CARMA) in California. Projected baseline lengths on Sgr A* ranged from $500 \times 10^6 \lambda$ on the shortest baseline to $3500 \times 10^6 \lambda$ on the longest. An effective bandwidth of 960 MHz was recorded, resulting in an aggregate recording data rate of 3.84 Gigabits/sec at each site (2 bits/sample, Nyquist sampling). Data were processed on the MIT Haystack Observatory Mark4 Correlator to produce complex visibilities with 0.5 second time resolution. Calibration quasars were robustly detected on all three baselines, validating operation of the VLBI array and allowing refinement of telescope positions for processing of the Sgr A* observations.

Because the geometry of VLBI baselines in an array is not typically known to $\ll 1\lambda$ precision, it is standard practise to search for detections over a grid of interferometric delay and delay-rate. A peak in signal-to-noise ratio of the visibility amplitude, found over a range of Nyquist-sampled delay and delay-rate space, is deemed a detection if the probability of false detection is sufficiently low. At an observing wavelength of 1.3mm, atmospheric turbulence limits the time over which the VLBI signal can be coherently integrated. Therefore, a technique of incoherent averaging (Rogers, Doeleman & Moran 1995) was used, which extends the effective integration time, but builds signal to noise more slowly than \sqrt{t} , to perform the fringe search over each 10 minute scan and determine the VLBI signal amplitude. After measuring the coherence losses due to atmospheric effects over a range of time scales, the atmospheric coherence time was found to be ~ 8 seconds, and the VLBI detection searches were thus made by incoherently averaging 8 second intervals of coherently averaged data. These searches resulted in robust detections and correlated flux density measurements of Sgr A* on both the SMT-JCMT SMT-CARMA baseline. No detections were found on the CARMA-JCMT baseline, which is attributable to the lower sensitivity of that baseline compared with the others. The error associated with each visibility amplitude was calculated by adding in quadrature the noise determined from the detection search with a 10% calibration

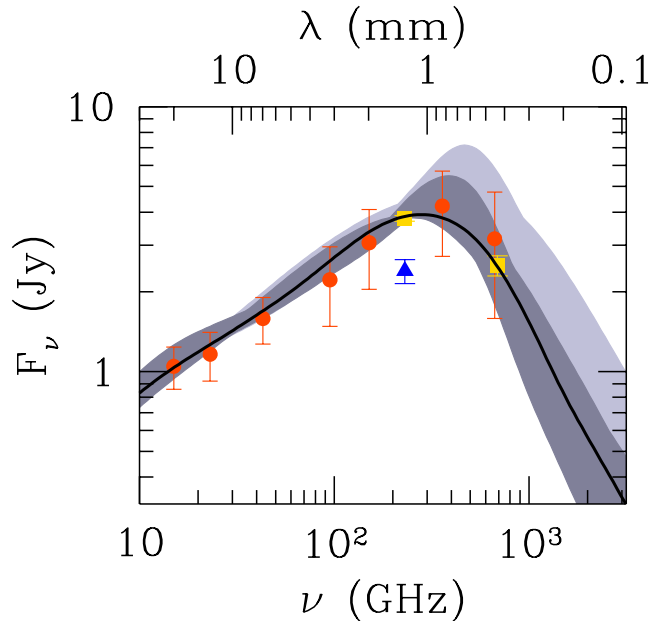


FIG. 1.— High-frequency radio data and the range of fitted model spectra. The red circles are taken from Yuan et al. (2004) (and references therein), the yellow squares are from Marrone (2006), and the blue triangle is the single-dish flux during the VLBI observations discussed here. Since all of the data points were not taken coincidentally errorbars on the radio data shown by the red circles are indicative of the variability, not the intrinsic measurement errors (in contrast to the yellow squares which were determined by coincident observations, and the blue triangle not used in the fit). The gray regions show the envelope of the model spectra, with the dark gray region showing $a \leq 0.9$, and the light gray showing $0.9 < a \leq 0.998$. Finally, the black line shows the spectrum for the spin and inclination shown in Fig. 2

error. Measurements of Sgr A* made with the CARMA array during the VLBI observations yield a total flux density of Sgr A* of 2.4 ± 0.25 Jy, which was observed to be stable over a time scale of hours. Errors in the total flux density measurement are dominated by pointing and calibration.

3. RIAF VISIBILITY MODELING

3.1. Accretion Flow Modeling

Sgr A* transitions from an inverted, optically thick spectrum to a optically thin one at millimeter wavelengths. This implies that Sgr A* is only becoming optically thin at 1.3 mm. Due to relativistic effects this transition does not occur isotropically for orbiting gas (e.g., Broderick & Loeb 2006a), becoming optically thin on the receding side at longer wavelengths than the approaching side of the accretion flows orbit. As a consequence, the opacity of the underlying accretion flow is crucial to imaging Sgr A*'s accretion flow.

Despite being diminutive in comparison to the Eddington luminosity for a $4.5 \times 10^6 M_\odot$ black hole, Sgr A* is still considerably bright, emitting a bolometric luminosity of approximately 10^{36} erg/s. Thus, it has been widely accepted that Sgr A* must be accretion powered, implying a minimum accretion rate of at least $10^{-10} M_\odot/\text{yr}$. It is presently unclear how this emission is produced. This is evidence by the variety of models that have been proposed to explain the emission characteristics of Sgr A* (e.g., Narayan et al. 1998; Blandford & Begelman 1999;

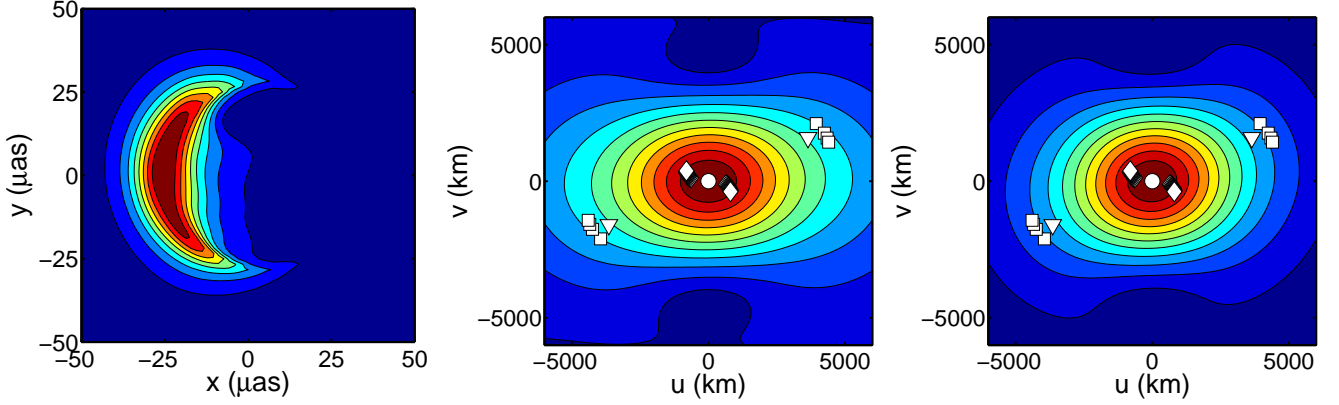


FIG. 2.— *Left:* An example image of the radiatively inefficient accretion flow around Sgr A* at 230 GHz, viewed at 60° from the black hole spin axis for a moderately rotating ($a = 0.5$) black hole. The image appears as a crescent due primarily to the Doppler beaming and shifting associated with the relativistic orbital velocities. The color-scheme is normalized such that red is bright, blue corresponds to vanishing intensity and the total flux from the image is 2.4 Jy . *Middle:* Visibility magnitudes associated with the image shown on top. For reference, the positions of the observations in the u - v plane are also shown by the white points (the circle, diamonds, & squares correspond to the single-dish, SMT-CARMA, & CARMA-JCMT detections, and the triangle corresponds to the JCMT-SMTO upper limit). *Right:* Scatter broadened visibility magnitudes. Again the u - v positions of the VLBI observations are shown.

Falcke & Markoff 2000; Yuan et al. 2002, 2003; Loeb & Waxman 2007). Models in which the emission arises directly from the accreting material have been subsumed into the general class of RIAFs, defined by the generally weak coupling between the electrons, which radiate rapidly, and the ions, which efficiently convert gravitational potential energy into heat (Narayan et al. 1998). This coupling may be sufficiently weak to allow accretion flows substantially in excess of the $10^{-10} M_\odot/\text{yr}$ required to explain the observed luminosity with a canonical radiative efficiency.

Nevertheless, the detection of polarization from Sgr A* above 100 GHz (Aitken et al. 2000; Bower et al. 2001, 2003; Marrone et al. 2006), and subsequent measurements of the Faraday rotation measure (Macquart et al. 2006; Marrone et al. 2007), has implied that the accretion rate near the black hole is significantly less than the Bondi rate, requiring the existence large-scale outflows (Agol 2000; Quataert & Gruzinov 2000). Therefore, in the absence of an unambiguous theory, we adopt a simple, self-similar model for the underlying accretion flow which includes substantial mass-loss.

For concreteness, we follow Yuan et al. (2003), and employ a model in which the accretion flow has a Keplerian velocity distribution, a population of thermal electrons with density and temperature

$$n_{e,\text{th}} = n_{e,\text{th}}^0 \left(\frac{r}{r_s} \right)^{-1.1} e^{-z^2/2\rho^2} \quad (1)$$

and

$$T_e = T_e^0 \left(\frac{r}{r_s} \right)^{-0.84}, \quad (2)$$

respectively, a population of non-thermal electrons

$$n_{e,\text{nth}} = n_{e,\text{nth}}^0 \left(\frac{r}{r_s} \right)^{-2.9} e^{-z^2/2\rho^2}, \quad (3)$$

and a toroidal magnetic field in approximate ($\beta = 10$) equipartition with the ions (which produce the majority of the pressure), i.e.,

$$\frac{B^2}{8\pi} = \beta^{-1} n_{e,\text{th}} \frac{m_p c^2 r_s}{12r}. \quad (4)$$

In all of these, $r_s = 2GM/c^2$ is the Schwarzschild radius, ρ is the cylindrical radius and z is the vertical coordinate. Inside of the innermost-stable circular orbit (ISCO) we assume the gas is plunging upon ballistic trajectories. In all of these expressions the radial structure was taken directly from Yuan et al. (2003) and the vertical structure was determined by assuming the disk height is comparable to ρ . Given a choice for the coefficients and a radiative transfer model, images may then produced using the fully-relativistic ray-tracing and radiative transfer schemes described in Broderick & Loeb (2006a) and Broderick & Loeb (2006b).

The primary emission mechanism is synchrotron, arising from both the thermal and non-thermal electrons. We model the emission from the thermal electrons using the emissivity described in Yuan et al. (2003), appropriately altered to account for relativistic effects (see, e.g., Broderick & Blandford 2004). Since we perform polarized radiative transfer via the entire complement of Stokes parameters, we employ the polarization fraction for thermal synchrotron as derived in Petrosian & McTiernan (1983). In doing so we have implicitly assumed that the emission due to thermal electrons is isotropic, which while generally not the case is unlikely to change our results significantly. For the non-thermal electrons we follow Jones & O'Dell (1977) for a power-law electron distribution, cutting the electron distribution off below a Lorentz factor of 10^2 and corresponding to a spectral index of $\alpha_{\text{disk}} = 1.25$, both roughly in agreement with the assumptions in Yuan et al. (2003). For both the thermal and non-thermal electrons the absorption coefficients are determined directly via Kirchoff's law.

To correct for the fact that Yuan et al. (2003) was a Newtonian study, we determine the three coefficients ($n_{e,\text{th}}^0$, T_e^0 and $n_{e,\text{nth}}^0$) by fitting the the average radio, sub-millimeter and near-infrared spectrum of Sgr A*. For every inclination and black hole spin presented here this was possible with extraordinary accuracy (reduce $\chi^2 < 1$ in all cases and $\lesssim 0.2$ for many), implying that this model is presently significantly under-constrained by

the quiescent spectrum alone⁵. This fit was performed at a number of points in the spin–inclination parameter space, yielding a tabulated set of coefficient values. Subsequently, we obtained the appropriate model parameters for arbitrary spins and inclinations via a high-order polynomial interpolation. The range of spectra for the models we employ here is presented in Fig. 1, together with the radio & sub-millimeter data that was used for the fitting procedure. The most deviant are the high-spin models, largely due to the interpolation process (and a direct consequence of the rapidly changing parameter values at $a \simeq 1$). These do not have substantially different images at 1.3 mm from their tabulated counterparts, and it is important to note that the associated error in the underlying RIAF model serves only to favor very high spins ($a \geq 0.99$), since in these cases it results in a larger accretion-flow photosphere and, as we shall see, the small size of the photosphere of the high-spin models is the primary reason they are excluded. Hence, in reality, such models are more strongly disfavored than shown here. All of these models are also capable of producing the Faraday rotation measures observed, and thus the polarimetric properties of Sgr A*.

At the time that Sgr A* was being monitored by Doeleman et al. (2008) it exhibited an anomalously low 1.3 mm flux of 2.4 ± 0.25 Jy, almost 40% below its average value (shown by the blue triangle in Fig. 1). To appropriately account for this we chose a “minimal” prescription for changing the model, reducing all densities by a fixed factor (decreasing the magnetic field such that β is fixed) until the observed flux was reproduced. In a sense, this models the low flux as a low-mass accretion period. These lower-density models do have noticeably smaller, though qualitatively similar, images compared to those used in the spectral fits.

An example image is shown in the left-panel of Fig. 2 for a moderate spin and viewing inclination. As seen in previous efforts to image relativistic accretion flows, the flow appears as a crescent associated with the approaching side of the accretion disk (Broderick & Loeb 2006a,b). The non-negligible optical depth obscures the black hole “silhouette” on this side. Due to both the Doppler beaming and the Doppler shift arising from the relativistic nature of the accretion flow at the inner-most portion of the accretion flow, the receding side is all but invisible.

Using this model we created a library of ideal-resolution images, each with a flux of 2.4 Jy, having different spins and viewing inclinations spanning all possible values.

3.2. Interstellar Electron Scattering

The existence of an interstellar scattering screen between Earth and the Galactic center has been well known for some time now. This has been carefully characterized empirically by a number of authors; we use the re-

⁵ However, part of the reason for this is almost certainly the fact that many of the radio fluxes were measured during different observational epochs, and thus the flux uncertainties are indicative of the source variability, not the intrinsic measurement error. For two of the data points in Fig. 1 (the yellow squares), this is not the case, having been measured coincidentally, and thus these play a much more significant role in constraining the RIAF model parameters.

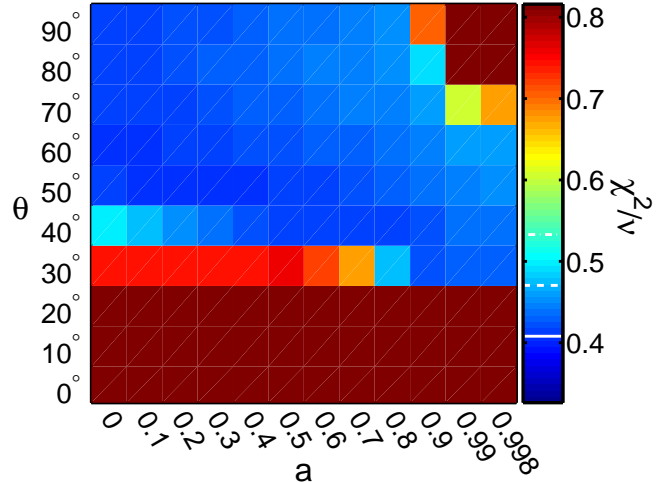


FIG. 3.— Effective reduced χ^2 for the best fit models in ξ and V_0 as a function of inclination and spin. For reference, white lines on the color-bar show the minimum χ^2 (solid), minimum $\chi^2 + 1$ (dashed) and minimum $\chi^2 + 2$ (dot-dashed). We were able to find a good fit for nearly all inclinations above 40° . Models with lower inclinations are too large at all ξ to produce the observed flux on the JCMT-SMTO baseline. Conversely, models with large inclinations and high spins were over-predict the fluxes on the SMTO-CARMA and CARMA-JCMT baselines.

cent model from Bower et al. (2006). In this the observed flux distribution is obtained by convolving the ideal flux with an anisotropic Gaussian scattering kernel. The anisotropic Gaussian is defined by the scattering widths along major and minor axes (both $\propto \lambda^2$) and the position angle of the minor axis (which is independent of λ). From Bower et al. (2006), these are

$$\sigma_{\text{maj}} = 0.56 \left(\frac{\lambda}{1 \text{ cm}} \right)^2 \text{ mas} \quad (5)$$

$$\sigma_{\text{min}} = 0.27 \left(\frac{\lambda}{1 \text{ cm}} \right)^2 \text{ mas} \quad (6)$$

with the minor axis oriented 70° North of East. In practice, the broadening was done in the u - v plane, where it reduces to a multiplicative factor.

3.3. Visibility Modeling

Visibilities are then defined in the normal way:

$$V(u, v) = \int dx \int dy e^{-2\pi i(xu + yv)/\lambda} I(x, y) \quad (7)$$

where $I(x, y)$ are the intensities on the image plane, with x aligned East-West and y North-South. Because changing the position angle, ξ , corresponds simply to a coordinate rotation, the images were originally computed only for a single position angle, namely $\xi = 0$. The visibilities associated with the ideal-resolution images were then computed, and subsequently rotated to the desired ξ . In practice, the visibilities were calculated via a Fast Fourier Transform, which was padded sufficiently to resolve the shortest baseline (SMTO-CARMA). We also vary the total flux, or equivalently $V_0 \equiv V(0, 0)$. For sufficiently different values a new image must be produced. However, for small variations around our canonical value of 2.4 Jy (within 0.5 Jy) simply renormalizing the visibilities produces a good approximation. Finally,

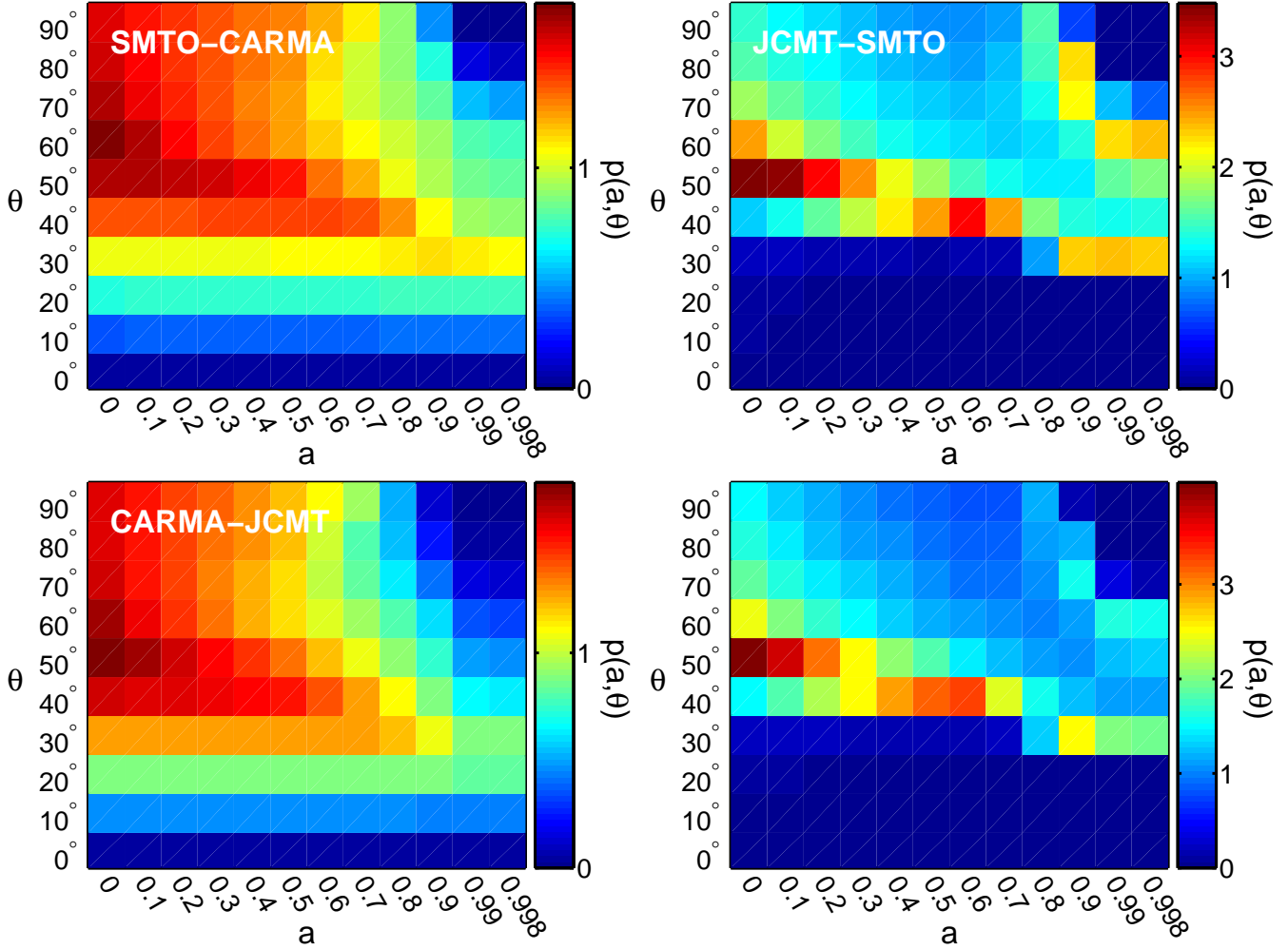


FIG. 4.— Probability densities of a given inclination and black hole spin for our canonical Sgr A* model. The *top left*, *top right* and *bottom left* panels show the contribution to $p(a, \theta)$ from the SMTO-CARMA, JCMT-SMTO and CARMA-JCMT baselines, after being marginalized over ξ and at the most-likely V_0 . The combined implied $p(a, \theta)$, marginalized over ξ and V_0 is shown in the *bottom right*. (Islands of high probability in the right panels are an artifact of under sampling the probability peak in inclination.) In each, $p(a, \theta)$ is normalized such that the average is unity, providing a clear sense of the significance of the variations in probability. Note that the color-scale is different in each panel. While the JCMT-SMTO measurement is clearly the most constraining, the other baselines are critical to eliminating high-inclination, high-spin solutions.

the interstellar-scatter broadening was effected by multiplying the visibilities in the u - v plane by the Fourier-transformed scattering kernel.

Since only Sgr A* was detected on only two of the three VLBI stations, there was insufficient observational data to determine the individual baseline visibility phases. Thus, henceforth, by visibility (and V) we shall, more properly, refer to the visibility magnitudes. These are necessarily a function of position in the u - v plane, the black hole spin (a), the spin inclination (θ), the position angle of the projected spin vector (ξ) and the flux normalization (V_0). That is, for a particular realization of the RIAF model, we have computed $V(u, v; a, \theta, \xi, V_0)$.

The ideal and broadened visibilities are shown in the center and right-panels of Fig. 2, respectively. In both of these the positions of the observed visibilities are shown by the white points. As expected, associated with the narrow-axis of the image crescent is a correspondingly broad feature in the visibilities. On the maximum scale of interest (the JCMT-SMTO baseline) the power is not substantially reduced by the interstellar electron scatter-

ing. At the same time, along the long-axis of the image crescent the visibilities drop off rapidly. Thus, we may expect that, at the very least, the VLBI observations will constrain ξ . This turns out to be correct.

4. BAYESIAN DATA ANALYSIS

We follow a Bayesian scheme to compute the probability that given the measured visibilities, a given set of model parameters (a, θ, ξ) are correct. This is, of course, predicated upon the assumption that our simplistic RIAF model is appropriate for Sgr A*. Indeed, this is the primary uncertainty in our reported constraints upon a , θ and ξ . While we can address this model dependence somewhat by comparing the results from different black hole masses, at this point we can only hope that our results are characteristic of generic RIAF models. This is not unreasonable given that the primary physics responsible for the structure of our images, the Keplerian velocity profile, is a common theme among RIAF models. Nevertheless, it remains to be proven.

Assuming the observational errors are Gaussian, the

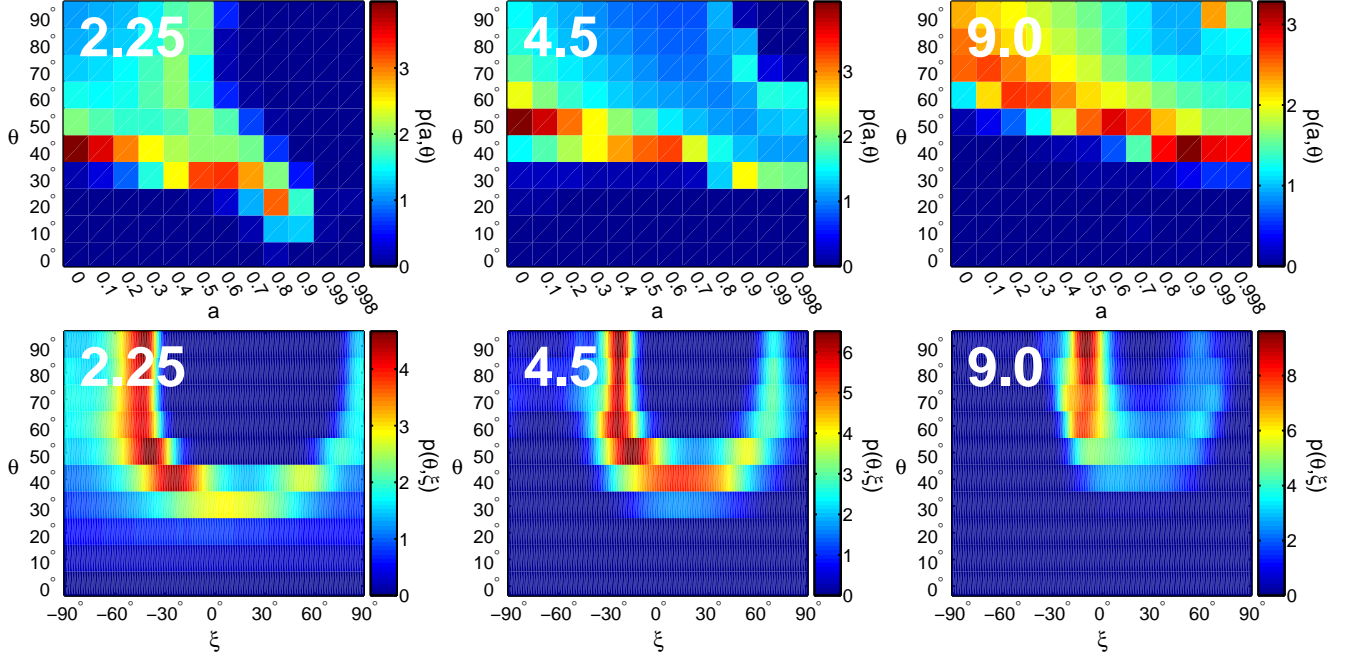


FIG. 5.— *Top*: Probability densities of a given inclination and black hole spin assuming that $M_{\text{SgrA}^*} = 2.25, 4.5$ and $9.0 \times 10^6 M_\odot$ (note that the best current estimate is $4.5 \pm 0.4 \times 10^6 M_\odot$). *Bottom*: Probability densities of a given inclination and position angle for the same masses. Note that the orientation of the accretion disk, and hence the black hole spin, is strongly constrained for all cases to lay in a taco-shell-shaped 2-dimensional surface within the inclination-spin-position angle parameter space. Regardless of mass, lower spins and moderate inclinations are preferred by the recent VLBI observations. A position angle of 0° corresponds to the projected spin vector being oriented North-South.

probability of measuring a visibility V_i *given* a particular set of model parameters (a, θ, ξ, V_0) is

$$P_i(V_i|a, \theta, \xi, V_0) = \frac{1}{\sqrt{2\pi}\Delta V_i} \exp \left\{ -\frac{[V_i - V(u_i, v_i; a, \theta, \xi, V_0)]^2}{2\Delta V_i^2} \right\} dV_i(s)$$

This is appropriate for detections, i.e., along the SMT-CARMA and JCMT-SMTO baselines. However, for the non-detection associated with the CARMA-JCMT baseline this is not the case. As discussed in Appendix A, the probability of a non-detection given a measurement threshold of V_i and intrinsic uncertainty of ΔV_i and expected value $V(u_i, v_i; a, \theta, \xi, V_0)$ is

$$P_i(< V_i|a, \theta, \xi, V_0) = \frac{1}{2} \left\{ 1 + \text{erf} \left[\frac{V_i - V(u_i, v_i; a, \theta, \xi, V_0)}{\sqrt{2}\Delta V_i} \right] \right\}. \quad (9)$$

Therefore, the probability of observing the measured set of independent visibilities *given* a particular RIAF model is

$$P(\{V_i\}|a, \theta, \xi, V_0) = \prod_{i=SC, JS} P_i(V_i|a, \theta, \xi, V_0) \times \prod_{j=CJ} P_j(< V_j|a, \theta, \xi, V_0), \quad (10)$$

where the first product is over the detections on the SMT-CARMA (*SC*) and JCMT-SMTO (*JS*) baselines, and the second is over the non-detections on the CARMA-JCMT (*CJ*).

In the absence of the non-detection, maximizing $P(V_i|a, \theta, \xi, V_0)$ corresponds to minimizing the normal

χ^2 . Even in the presence of the non-detection, however, we can define an effective χ^2 by

$$\chi^2 = -2 \ln \left[P(\{V_i\}|a, \theta, \xi, V_0) \right] + \ln \left(\prod_i 2\pi \Delta V_i^2 \right), \quad (11)$$

which reduces to the standard definition if all the measurements constitute detections. Note that since only one of the visibility measurements is an upper limit, we may expect that this definition of χ^2 will behave very similarly to the standard definition in our case. The reduced effective χ^2 is shown as a function of spin and inclination in Fig. 3 for the best fit V_0 and ξ . For nearly all inclinations above 35° a good fit can be found (indeed, $\chi^2/\nu \simeq 0.4!$). The exception is at very high spins and high inclinations (where the disk is edge on).

While we now have the probability that the observed visibilities come from a given model, what we would like to know is somewhat different: the probability of a set of model parameters given the observed visibilities. That is, we would like the probability density $p(a, \theta, \xi, V_0|\{V_i\})$. With an appropriate choice of priors on a, θ, ξ and V_0 , we may construct the desired probabilities via Bayes' theorem. As such, we now turn to the problem of choosing these priors.

A natural choice for the prior upon θ and ξ comes from the assumption that Sgr A*'s spin orientation probability is isotropic, i.e., we have no other information regarding its direction. This results in $\wp(\theta, \xi) = \sin \theta$. In the absence of a complete theoretical understanding of the spin evolution of supermassive black holes, we choose the prior on a to be uniform, i.e. $\wp(a) = 1$. Finally, we set the prior on V_0 to be uniform as well. Since the allowed range of variation in V_0 is small, and the prior probabil-

ity is expected to vary smoothly, this is not a significant oversight. Therefore, Bayes' theorem gives

$$\begin{aligned} p(a, \theta, \xi, V_0 | \{V_i\}) &= \frac{P(\{V_i\} | a, \theta, \xi, V_0) \wp(a) \wp(\theta, \xi) \wp(V_0)}{\int da d\theta d\xi dV_0 P(\{V_i\} | a, \theta, \xi, V_0) \wp(a) \wp(\theta, \xi) \wp(V_0)} \\ &= \frac{P(\{V_i\} | a, \theta, \xi, V_0) \sin \theta}{\int da d\theta d\xi dV_0 P(\{V_i\} | a, \theta, \xi, V_0) \sin \theta}. \end{aligned} \quad (12)$$

This is necessarily a probability density in a four-dimensional parameter space, and thus is quite difficult to visualize directly. Furthermore, some of these parameters are physically more interesting than others. Therefore, we construct a variety of marginalized probabilities from this for presentation and analysis. The most general is simply marginalized over V_0 :

$$p(a, \theta, \xi) = \int dV_0 p(a, \theta, \xi, V_0 | \{V_i\}). \quad (13)$$

This probability distribution is shown explicitly in Fig. 6. We construct a pair of two-dimensional marginalized probability densities as well:

$$p(a, \theta) = \int d\xi dV_0 p(a, \theta, \xi, V_0 | \{V_i\}) \quad (14)$$

and

$$p(\theta, \xi) = \int da dV_0 p(a, \theta, \xi, V_0 | \{V_i\}) \quad (15)$$

These are plotted in Fig.'s 4 and 5. Alternatively, we could choose the most likely values of either V_0 or ξ . For some of the panels in Fig. 4, we choose a hybrid probability: marginalized over ξ but the most likely in V_0 . Finally, for the purpose of identifying the probability distribution of each parameter separately, we also construct the marginalized one-dimensional probability densities:

$$p(a) = \int d\theta d\xi dV_0 p(a, \theta, \xi, V_0 | \{V_i\}) \quad (16)$$

$$p(\theta) = \int da d\xi dV_0 p(a, \theta, \xi, V_0 | \{V_i\}) \quad (17)$$

$$p(\xi) = \int da d\theta dV_0 p(a, \theta, \xi, V_0 | \{V_i\}). \quad (18)$$

These are shown in Fig 7.

5. THE NATURE OF THE VLBI CONSTRAINTS

The relative importance of the three different baselines is shown in Fig. 4. To make a direct comparison of the contributions from different baselines possible, the top-left, top-right and bottom-left panels of Fig. 4 show the probability after setting V_0 to the most likely value and marginalizing over ξ (justified by the fact that the probability distributions in ξ are quite similar, while those in V_0 were not). Both the SMTO-CARMA detections and the CARMA-JCMT upper limit exclude the high-spin, high-inclination portion of the parameter space. This is primarily because high-spin RIAF models result in images that are sufficiently compact to substantially overpredict the flux observed on both of these baselines. Due to its considerably longer baseline length, the CARMA-JCMT non-detection is more constraining than the multiple SMTO-CARMA detections, despite only representing an upper-limit.

As anticipated, most constraining are the visibilities measured on the JCMT-SMTO baseline. This baseline convincingly excludes low inclinations (face-on disks). This may be easily understood, qualitatively, in terms of the RIAF images themselves. As inclination increases, the RIAF image becomes more asymmetric, and increasingly dominated by a thin crescent (e.g., left-panel of Fig. 2). It is the generally the direction across the minor-axis of the crescent that has the shortest scale intensity variations, and consequently determines the long-baseline visibilities. Below a critical inclination, the crescent grows sufficiently fat that it is resolved out by the JCMT-SMTO baseline.

At large inclinations, the crescent becomes too thin, requiring the JCMT-SMTO baseline to be oriented obliquely relative to the spin axis of Sgr A*. This restricts the available values of ξ to an increasingly limited range, as may be seen explicitly in the bottom-center panel of Fig. 5. Thus, while it is nearly always possible to obtain a satisfactory fit, the reduced range in position angle makes such a configuration unlikely. Hence we find that the long-baseline visibilities strongly constrain the possible values of inclination and spin to a narrow band near $\theta \simeq 50^\circ$ and generally favoring moderate a . We note that the appearance of islands of high probability in the top-right panel of Fig. 4 is almost certainly due to under sampling in θ near this critical region, and not indicative of a bifurcation in the allowed parameter space.

This behavior is clearly visible in the combined $p(a, \theta)$, which closely resembles that from the JCMT-SMTO baseline alone. In this case, we have marginalized over V_0 as well as ξ (i.e., $p(a, \theta)$ as defined by eq. 14), though the difference had we chosen the most likely value of V_0 is less than 10% everywhere. The shorter baselines have effectively removed a small high-spin, high-inclination island that persisted in the JCMT-SMTO probability distribution alone. Additionally, they have further restricted the spin to low-to-moderate levels. The combined result, however, is to restrict the spin and inclination to a narrow strip.

In a similar fashion, $p(\theta, \xi)$ appears to limit RIAF models to a narrow band of orientations. Due to the approximate up-down symmetry of the image (parallel to the projected spin axis), the corresponding band has a characteristic "U" shape, corresponding to something akin to a taco shell in the a, θ, ξ parameter space. (Note that we do not plot ξ over the entire 360° range due to the symmetry of the visibilities under reflection.)

In order to ascertain how the present uncertainty in the mass of Sgr A* effects our conclusions, we repeated the analysis for black hole masses of $4.1 \times 10^6 M_\odot$ and $4.9 \times 10^6 M_\odot$. Since the mass uncertainty is strongly correlated with the distance to Sgr A* ($MD^{-1.8}$ is very well determined by stellar orbits, Ghez et al. 2008), we altered the distance to the Galactic center accordingly. As a consequence, the roughly 10% change in the mass results in a 4% change in the angular scale of the RIAF images. A correspondingly small change was seen in the resulting probability distributions, implying that, apart from the the RIAF modeling, the paucity of millimeter-VLBI observations is the dominant obstacle to constraining the black hole spin properties.

Altering the angular scale of the images also provides a proxy, albeit a poor one, for considering different Sgr

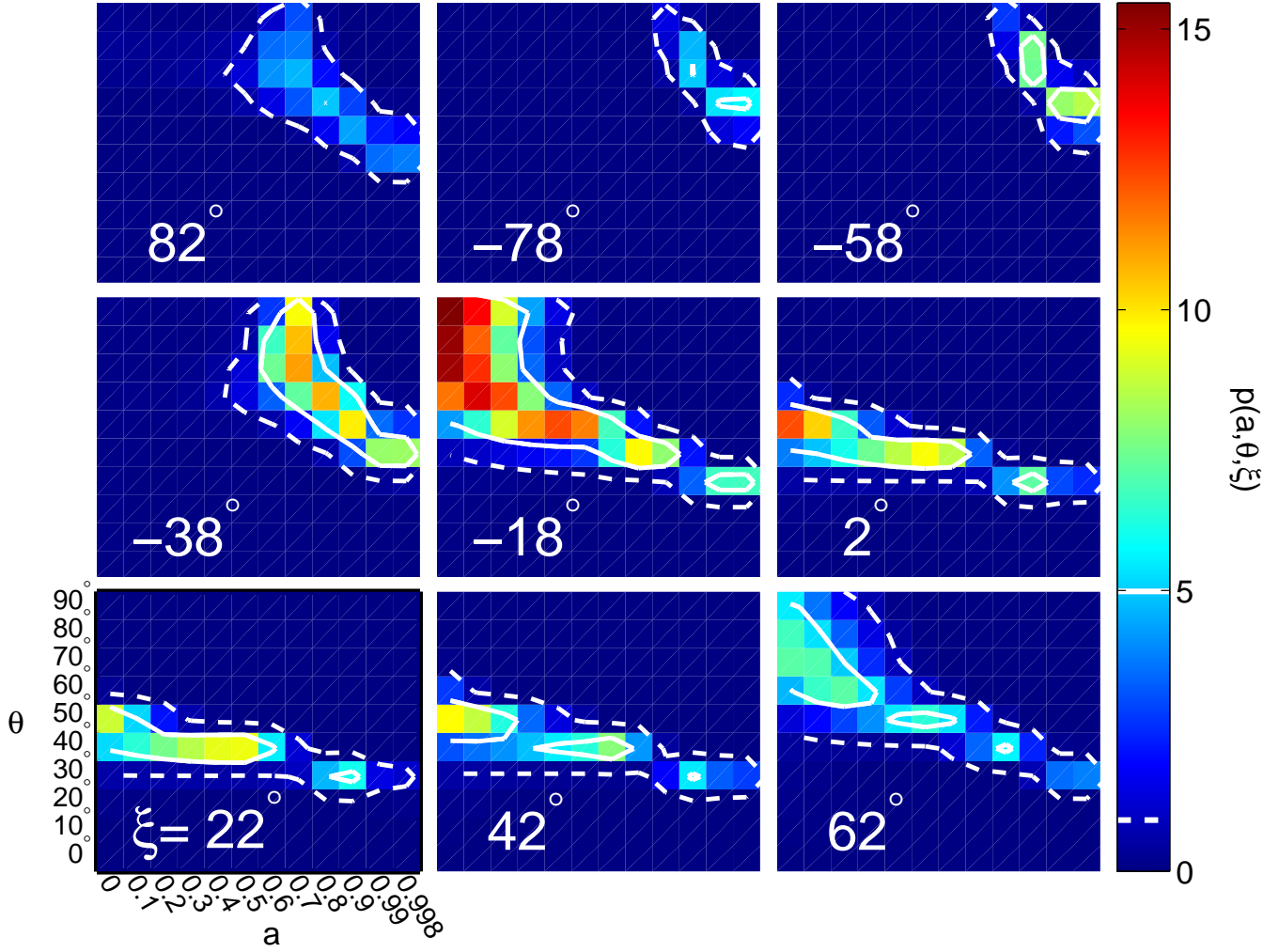


FIG. 6.— $p(a, \theta, \xi)$ is shown for slices of constant ξ . The slice with the maximum over-all probability is shown in the center panel. The white solid and dashed lines show the $1\text{-}\sigma$ and $2\text{-}\sigma$ contours, defined explicitly in the text, respectively. Note that while the probability is quite peaked, likely values of the parameters exist for a large number of spins, inclinations and position angles.

A* models, corresponding to different disk scale lengths. $p(a, \theta)$ and $p(\theta, \xi)$ for a black holes of mass $2.25 \times 10^6 M_\odot$ and $9.0 \times 10^6 M_\odot$ are compared to those determined using the estimated value of $4.5 \times 10^6 M_\odot$ in Fig. 5. These extreme mass changes correspond to a 30% change in the angular mass scales of the images, and can make a substantial difference to the resulting probability distributions. Nevertheless, low inclinations and spins are still generally preferred, though less so for large images.

Finally, because Sgr A* is an inherently dynamical environment, exhibiting substantial variations in the millimeter flux on 30 min time scales, we may not be justified in assuming that the image of Sgr A* was stationary during the entire time that observations were made. Indeed, searching for variations in the VLBI closure quantities has been suggested as a way to directly probe the existence of hot spots in Sgr A*'s accretion flow (Doeleman et al. 2008). Therefore, to check this, we repeated this analysis for the two days over which the observations were performed separately, finding no significant difference. This implies that either Sgr A* was quiescent during this time or that the individual 3.5 hr observation windows were sufficiently long to average out this activity. The anomalously low 1.3 mm flux suggests the

former interpretation is correct.

6. PARAMETER ESTIMATION

It is evident from the previous section that the allowed parameter space is highly non-Gaussian. As such, we must take special care in how we extract values and their attendant uncertainties for the fitting parameters. In all cases, these values will be highly correlated, and the systematic uncertainties due to the choice of a particular RIAF model will dominate the errors (and thus will not be reviewed again in this section).

In order to determine $1\text{-}\sigma$ and $2\text{-}\sigma$ error surfaces, we first define a cumulative probability

$$P(> p) = \int_{p(\mathbf{x}) \geq p} p(\mathbf{x}) d\mathbf{x} \quad (19)$$

where \mathbf{x} are the parameters of the total probability distribution. That is, $P(> p)$ is simply the probability associated with the region of the parameter space that has probability density above p . This is necessarily a monotonic function of p , which may then be inverted to find p as a function of $P(> p)$. We then define the $1\text{-}\sigma$ contour to be that associated with the p for which $P(> p) = 0.683$. Similarly, we define the $2\text{-}\sigma$ contour by

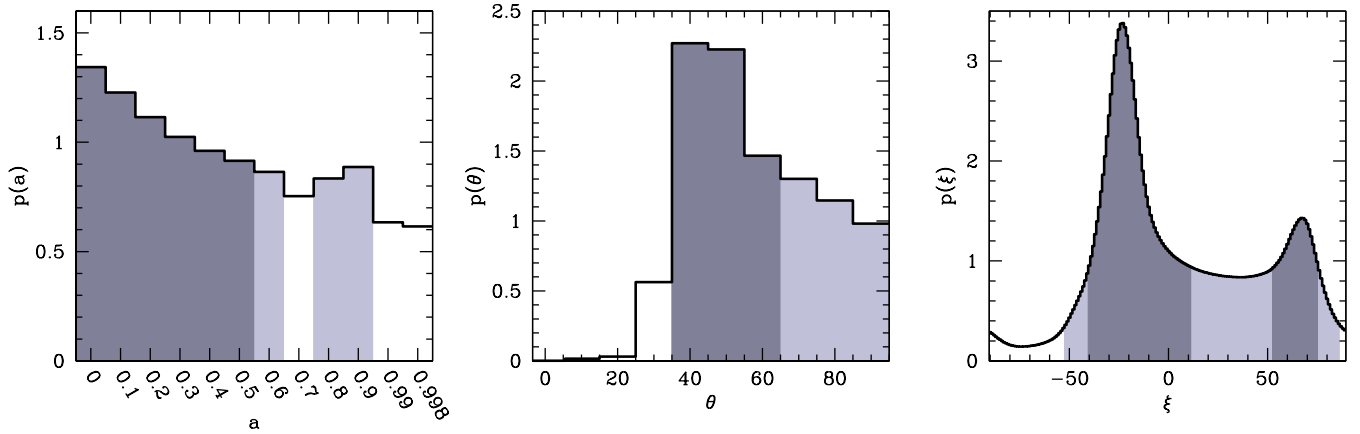


FIG. 7.— From left to right: $p(a)$, $p(\theta)$ and $p(\xi)$, all marginalized over all other parameters. In all cases the probability distribution is highly non-Gaussian. The dark and light shaded regions denote the 1- σ and 2- σ regions, as defined in the text, respectively. It is important to keep in mind that parameter estimates from these distributions are strongly correlated.

$P(> p) = 0.954$. While these satisfy the normal definition of 1- σ and 2- σ errors, it is important to remember that in our case the errors are strongly non-Gaussian.

Fig. 6 shows the probability density in the full three-dimensional parameter space as a sequence of constant- ξ slices. The most likely parameter combination is $a = 0^{+0.2+0.4}$, $\theta = 90^\circ_{-40^\circ-50^\circ}$ and $\xi = -18^\circ_{-8^\circ-12^\circ}$. However, as remarked in the previous section, there are acceptable solutions for a wide range of a , θ and ξ . The primary effect of the VLBI measurements is to restrict these parameters to a band around a two-dimensional surface, resembling a taco shell with its sides around $\xi \simeq -23^\circ$ and $\xi \simeq 67^\circ$, the highest probability densities clustered on the former. Generally, we see a preference for low spins and can rule out inclinations below 30° .

More diagnostic for single parameters are the fully marginalized probability distributions shown in Fig. 7. It must be remembered, however, that these parameter estimates are strongly correlated, and thus these estimates should be used with caution. Again we use the cumulative probability, $P(> p)$ to define the 1- σ and 2- σ surfaces, shown in the panels of Fig. 7 as the dark and light shaded regions, respectively.

From the left panel of Fig. 7, the most likely spin is $a = 0^{+0.6+0.9}$. While we can rule out very high spins ($a \geq 0.99$) at the 2- σ level for our particular RIAF model, the spin is otherwise weakly constrained. Moreover, it appears to have a small high-spin island, at the 2- σ level, around $a = 0.8$ – 0.9 . The presence of this island is limited by the CARMA-JCMT non-detection, and therefore can be directly probed via future observations.

In contrast, the inclination is fairly robustly limited. The most likely inclination is $\theta = 40^\circ_{-20^\circ-50^\circ}$, where the lopsided errors are due to the lopsided nature of the probability distribution. It is very clear in the center panel of Fig. 7 that face-on geometries ($\theta \leq 30^\circ$) are convincingly ruled out. However, there is a tail extending to higher inclinations⁶.

The distribution of position angles is more complicated than either spin or inclination. In the right panel of Fig. 7 we see the taco-shell geometry most clearly in

terms of the bimodal distribution of likely ξ . The most probable position angle is $\xi = -23^\circ_{-17^\circ-29^\circ}^{+35^\circ+110^\circ}$. However, a second solution does exist at $\xi = 67^\circ_{-15^\circ-119^\circ}^{+8^\circ+19^\circ}$, though containing only 29% of the probability (under the 1- σ peak) of the more likely solution.

7. CONCLUSIONS

Despite the sparse u - v coverage, and the existence of a detection on only one long baseline, we have been able to significantly constrain the possible parameters of an accretion flow onto Sgr A*. Within the context of a qualitative RIAF model that fits the observed spectra of Sgr A*, we have been able to substantially constrain the orientation of Sgr A*'s spin. The magnitude of this spin is less well determined, though the black hole cannot be maximally rotating. This result is relatively insensitive to the black hole mass.

We have not ascertained the strength of our constraints' dependence upon the particular RIAF model. However, there are two reasons to believe that our results will be generic for most RIAF models. The first is that the underlying physics that limits the orientation is the Doppler beaming and boosting that is dependent primarily upon the Keplerian velocity profile of the accretion flow, a feature that is generic among most RIAF models. The second is the weak dependence upon large variations in mass, implying that changing the scale lengths of the accretion model does little to alter our results. Thus, we expect the qualitative form of our constraints to be a generic feature of all RIAF models for Sgr A*, and our quantitative results to be roughly correct. Of course, should the emission observed from Sgr A* not arise in an accretion flow, our results could be quite different.

As implied by the right-panel of Fig. 2, additional long-baseline observations are sorely needed to unambiguously determine both the applicability of RIAFs to Sgr A* and constrain their parameters. In a companion paper, Fish et al. (2008) we will report upon an analysis of the ability of possible millimeter VLBI arrays to do so. Given the number of potential radio telescopes that could be added to the current 1.3mm VLBI array (Doeleman et al. 2008), the prospects for making significant progress in model parameter estimation are excellent. However, at

⁶ Indeed, as mentioned above, the most likely overall set of parameters has $\theta = 90^\circ$.

this point, it is clear that with the advent of millimeter VLBI we are now entering an era of precision black-hole accretion physics.

APPENDIX

NON-DETECTION PROBABILITY

Consider an observable y , with an expected value of y_0 and Gaussian random errors of amplitude Δy . Then, the probability density of measuring a value y is

$$p(y) = \frac{e^{-(y-y_0)^2/2\Delta y^2}}{\sqrt{2\pi}\Delta y}. \quad (\text{A1})$$

A non-detection, by definition, corresponds to a “measured” value of y below some threshold Y . The probability of such an event is simply

$$P(< Y) = \int_{-\infty}^Y p(y)dy = \frac{1}{2} + \int_{y_0}^Y \frac{e^{-(y-y_0)^2/2\Delta y^2}}{\sqrt{2\pi}\Delta y} dy = \frac{1}{2} \left[1 + \operatorname{erf} \left(\frac{Y - y_0}{\sqrt{2}\Delta y} \right) \right], \quad (\text{A2})$$

where

$$\operatorname{erf}(x) \equiv \sqrt{\frac{2}{\pi}} \int_0^x e^{-t^2} dt, \quad (\text{A3})$$

is the standard error-function. As expected, when $Y = y_0$, $p(< y_0) = 1/2$ and when $Y \gg y_0$, $p(< y_0) \simeq 1$.

REFERENCES

- Agol, E. 2000, 538, 121
Aitken, D. K., et al. 2000, ApJ, 534, L173
Blandford, R. D. & Begelman, M. C. 1999, MNRAS, 303, L1
Bower, G. C., Write, M. C. H., Falcke, H. & Backer, D. C. 2001, ApJ, 555, 103
Bower, G. C., Write, M. C. H., Falcke, H. & Backer, D. C. 2003, ApJ, 588, 331
Bower, G. C., Goss, W. M., Falcke, H., Backer, D. C. & Lithwick, Y. 2006, ApJ, 648, L127
Broderick, A. & Blandford, R. 2003, MNRAS, 342, 1280
Broderick, A. E. & Blandford, R. D., MNRAS, 349, 994
Broderick, A. E. & Loeb, A. 2005, MNRAS, 363, 353
Broderick, A. E. 2006, MNRAS, 366, L10
Broderick, A. E. & Loeb, A. 2006a, ApJ, 636, L109
Broderick, A. E. & Loeb, A. 2006b, MNRAS, 367, 905
Broderick, A. E., Loeb, A. & Narayan, R. 2008, (*submitted*)
Broderick, A. E. & Narayan, R. 2006, ApJ, 638, L21
Doeleman et al. 2008, Nature, 455, 78
Doeleman, S. S., Fish, V. L., Broderick, A. E., Loeb, A. & Rogers, A. E. E. 2008, ApJ, (*submitted*, *arXiv:0809.3424*)
Falcke, H. & Markoff, S. 2000, *ã*, 362, 113
Fish, V. L. et al. 2008, ApJ, (*submitted*, *arXiv:0809.4489*)
Ghez, A. M. et al. 2008, ApJ, (*in press*, *arXiv:0808.2870*)
Jones, T. W. & O’Dell, S. L. 1977, ApJ, 214, 522
Loeb, A. & Waxman, E. 2007, JCAP, 3, 11
Macquart, J.-P. et al. 2006, ApJ, 646, 111
Marrone, D. P. 2006, Ph.D. thesis, Harvard Univ.
Marrone, D. .P., Moran, J. M., Zhao, J.-H. & Rao, R. 2006, Journal of Physics Conference Series, 54, 354
Marrone, D. .P., Moran, J. M., Zhao, J.-H. & Rao, R. 2007, ApJ, 654, 57
Narayan, R., Mahadevan, R., Grindlay, J. E., Popham, R. G. & Gammie, C. 1998, ApJ, 492, 554
Petrosian, V. & McTiernan, J. M. 1983, Phys. Fluids, 26, 3023
Quataert, E. & Gruzinov, A. 2000, ApJ, 545, 842
Rogers, A.E.E, Doeleman, S. & Moran, J.M. 1995, AJ, 109, 1391
Yuan, F., Markoff, S. & Falcke, H. 2002, *ã*, 383, 854
Yuan, F., Quataert, E. & Narayan, R. 2003, ApJ, 598, 301
Yuan, F., Quataert, E. & Narayan, R. 2004, ApJ, 606, 894